Available online at www.sciencedirect.com
SCIENCE DIRECT®
Journal of Magnetic Resonance 170 (2004) 299–309
JMR Journal of Magnetic Resonance
www.elsevier.com/locate/jmr

Reconstruction of porous material geometry by stochastic optimization based on bulk NMR measurements of the dipolar field

Louis-S. Bouchard, Warren S. Warren*

Department of Chemistry, Princeton University, Princeton, NJ 08544, USA

Received 16 April 2004; revised 23 May 2004
Available online 14 August 2004

Abstract

The dependence of the bulk signal intensity from a CRAZED NMR pulse sequence on magnetic field gradient strength and direction as a method to probe the geometry of porous materials is investigated. In this article, we report on the reconstruction of three-dimensional media consisting of a void phase and an NMR-observable liquid phase using the bulk intensity of the distant dipolar field. The correlation gradient strength and direction provide the spatial encoding of the material geometry. An integral equation for the total signal intensity is then solved numerically by a simulated annealing algorithm to recover the indicator function of the fluid phase. Results show that cylindrical and spherical structures smaller than the volume contributing to the NMR signal can be resolved using three values of the correlation distance and three orthogonal gradient directions. This is done by minimizing a cost function which measures the distance between the bulk signal dependence on gradient parameters for the simulated configuration and the signal dependence for the target configuration. The algorithm can reconstruct and differentiate their spherical and cylindrical phase-inverted equivalents. It can also differentiate horizontal from vertical cylinders, demonstrating the potential for assessing structural anisotropy and other coarse geometric quantifiers in a porous material.

Keywords: Intermolecular multiple-quantum coherences; Distant dipolar field; Porous materials; Inverse problem; NMR

1. Introduction

Magnetic resonance imaging has become an important and versatile technique for determining material structure, both in vivo and in vitro. In principle, resolution is generally limited by the available magnetic field gradient strength (spins are resolvable if the gradient separates their frequencies by more than the intrinsic linewidth) but in practice, the inherent low sensitivity and limited scan time (particularly in vivo) normally provides the more fundamental limitation. As a result, individual image voxels are usually much larger (typically 100 μm–1 mm) than cellular dimensions.

Methods for extracting limited information on shorter distance scales have proven very useful. Diffusion provides a natural discriminant over very short distances. In bulk water, molecules diffuse isotropically, with rms motion of approximately 7 μm in any specific direction over 10 ms. Water diffusion in tissue is typically both slower and anisotropic, reflecting local structure on a micron distance scale. This variation is generally measured by methods such as diffusion tensor imaging (DTI) and has turned out to be clinically useful. However, there is still a significant gap between the distances probed by DTI and those resolved in typical in vivo images. These limitations are particularly severe when material inclusions or pores are too large to be probed by pulsed-field gradient diffusion methods, as happens for example in as-

* Corresponding author. Fax: +1 609 258 6746.
E-mail address: wwarren@princeton.edu (W.S. Warren).

1090-7807/$ - see front matter © 2004 Published by Elsevier Inc.
doi:10.1016/j.jmr.2004.05.023

sessments of rock structure, trabecular bone quality, and tumor vessel topology.

Intermolecular multiple-quantum coherences (iMQCs) or distant dipolar field (DDF) measurements have been proposed as a method for probing materials microstructure [1,2], and to obtain sub-voxel resolution in MRI and fMRI [3]. Measurements of the signal intensity as function of the correlation gradient strength in a CRAZED experiment were shown to depend on material microstructure, and that the technique is most suited for distances of tens to hundreds of microns. In particular, it should be possible to obtain simple geometric quantifiers in biological or porous media on those length scales. Thus, it complements DTI and direct measurements [4]. We have shown recently [5] that variation of the gradient strength and direction can probe structural anisotropy in trabecular bone.

Here we explore the theoretical limitations of the iMQC method. Specifically, we address the inverse problem of reconstructing the material geometry from iMQC measurements. We show that, at least for simple geometries, it is generally possible to reconstruct microstructural information from a series of iMQC measurements, exploiting different gradient strengths and directions. This implies that iMQC images can provide contrast which complements all other MRI methods. Using three values of the correlation distance and three orthogonal gradient directions, we show that this simple method can reconstruct and differentiate cylindrical from spherical geometries, and their phase-inverted equivalents. Results from the reconstruction are sufficient for computing simple statistical descriptors of the geometry.

1.1. Theory

Let the region of three-dimensional space corresponding to the NMR sample volume be denoted $S(S \subset \mathbb{R}^3)$. Consider a material with a solid phase, $V \subset S$, and an NMR-active liquid phase $U \subset S$. The sets U, V are compact in $\mathbb{R}^3$, $V \cap U$ has measure 0, and let $\chi_U(\mathbf{r})$ denote the indicator function of the liquid phase:

$$\chi_U(\mathbf{r}) = \begin{cases} 1 & \mathbf{r} \in U, \\ 0 & \mathbf{r} \notin U, \end{cases} \tag{1}$$

and analoguously for $\chi_V(\mathbf{r})$, the indicator function for the solid phase. The equilibrium magnetization density can be written as $\chi_U(\mathbf{r})M_0^U + \chi_V(\mathbf{r})M_0^V$, M_0^U is the equilibrium magnetization density of the liquid phase, M_0^V is for the solid phase. We consider biphasic materials ($M_0^V = 0$), and we are interested in the behavior of the NMR signal following a double-quantum CRAZED (iDQC) pulse sequence, as shown in Fig. 1.

In the rotating wave approximation, the y-component of the signal at $t = 0$ emitted by the entire liquid phase, for this pulse sequence, is given by (see Appendix A):

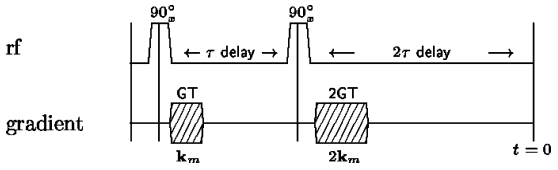

Fig. 1. Pulse sequence diagram for CRAZED iDQC experiment. The strength G, duration T and direction of the gradient pulses is expressed by the wave vectors $\mathbf{k}_m$ and $2\mathbf{k}_m$.

$$T_y(\mathbf{k}) = \int_U \int_U \chi_U(\mathbf{r})\chi_U(\mathbf{r}')K(\mathbf{r},\mathbf{r}')\cos(\mathbf{k}\cdot\mathbf{r}) \times [\sin(\mathbf{k}\cdot\mathbf{r}') - \sin(3\mathbf{k}\cdot\mathbf{r}')]\,\mathrm{d}^3\mathbf{r}'\,\mathrm{d}^3\mathbf{r}, \tag{2}$$

where the integration kernel $K(\mathbf{r},\mathbf{r}')$ is $(3\cos^2\theta - 1)/2|\mathbf{r} - \mathbf{r}'|^3$. Similar expressions are obtained for the x-component (see Appendix A), or for arbitrary pulse phases, flip angles, and in general, the functional form is the same: $\iint \chi(\mathbf{r})\chi(\mathbf{r}')f(\mathbf{r},\mathbf{r}')\,\mathrm{d}^3\mathbf{r}'\,\mathrm{d}^3\mathbf{r}$. The problem of solving for the material geometry amounts to solving for the indicator function $\chi_U(\mathbf{r})$ in the integrand.

The y-component of the signal, $T_y(\mathbf{k})$, is an observable which is a function of the wave vector $\mathbf{k}$. The wave vector is selected by adjusting the area and direction of the gradient pulses. While there exists no analytic solutions to this integral equation in the general case, we are led to consider numerical approximations. An exact solution over a three-dimensional grid of size N^3 requires N^6 NMR measurements for different values of the wave vector to give a soluble system of equations.[1] We would like to use grid sizes of order 32^3 or better to differentiate basic geometries, however, each NMR measurement takes a little more than a minute to acquire because of the long relaxation times of liquids, and so the acquisition of 32^6 points would take over 2000 years. In this article, we demonstrate that the simulated annealing algorithm of Kirkpatrick [6] can be adapted for reconstructing simple geometries on 8^3, 16^3, and 32^3 grids using far fewer data points.

1.2. Algorithm

The geometry of a material is reconstructed using knowledge of its signal dependence on correlation gradient strength and direction. In principle, these could be NMR measurements performed by measuring the bulk signal intensity (modulus) for a CRAZED sequence as function of several values of the wave vector $\mathbf{k}_1, \mathbf{k}_2, \ldots, \mathbf{k}_{n_k}$. If we know the theoretical dependence of the signal on material geometry, for example suppose that the simple model of Eq. (2) holds, we can then guess the indicator function, compute the signal dependence

[1] Discretization of the domain $U \cup V$ into N^3 gridpoints produces N^3 possible values for the indicator function (one for every gridpoint). However, the product $\chi(\mathbf{r})\chi(\mathbf{r}')$ gives $(N^3)^2$ unknowns $\chi(\mathbf{r}_i)\chi(\mathbf{r}_j)$.

as function of wave vector and compare to the experimental data. A fictitious energy can be used to measure the deviation from the true material geometry and to evolve the indicator function towards the optimal configuration. In this article, the experimental measurements are generated by using Eq. (2) and the analogous expression for $T_x(\mathbf{k})$ to calculate the NMR signal for a given "target geometry" for 3 values of the correlation distance and 3 orthogonal gradient directions, i.e., $n_k = 9$ values of the wave vector. We call the modulus $TM(\mathbf{k}) = [T_x^2(\mathbf{k}) + T_y^2(\mathbf{k})]^{1/2}$ the "target NMR signal," since it is obtained from the target geometry we wish to reconstruct. The volume fraction of the liquid phase of the target geometry is denoted ϕ.

We take $U \cup V$ to be a rectangle $[0,1]\times[0,1]\times[0,1]$ and consider a 32^3 cartesian grid of evenly spaced points with indicator function for the fluid phase defined at every node and denoted by $\chi_{ijk}(i,j,k$ range over the integers 1–32). Consider a sequence of random variables $\xi = (\xi_0, \ldots, \xi_n)$ with values in the (finite) set X. The phase space X is taken to be the set of all possible indicator functions χ_{ijk} subjected to the constraint that the sum $32^{-3}\sum_{i,j,k}\chi_{ijk}$ must equal the volume fraction ϕ for the liquid phase. Let Ω, the set of possible outcomes, be given by:

$$\Omega = \{\omega : \omega = (x^{i_0}, \ldots, x^{i_n}), x^i \in X\} \tag{3}$$

and for each $\omega = (x^{i_0}, \ldots, x^{i_n})$ put

$$p(\omega) = \mu_0(x^{i_0})p_1(x^{i_0}, x^{i_1}) \ldots p_n(x^{i_{n-1}}, x^{i_n}). \tag{4}$$

The set of probabilities $p(\omega)$ generates a probability measure P on the σ-algebra containing all subsets of Ω, where $\mathsf{P}(\xi_0 = x^{i_0}) = \mu_0(x^{i_0})$ is the initial distribution ($\sum_i \mu_0(x^i) = 1, 0 \leqslant \mu_0(x^i) \leqslant 1$) and the conditional probability

$$\mathsf{P}(\xi_{k+1} = x^{i_{k+1}} \mid \xi_k = x^{i_k}) = p_k(x^{i_k}, x^{i_{k+1}}) \tag{5}$$

defines a stochastic matrix for the transition from state x^{i_k} to state $x^{i_{k+1}}$ at time k. The initial distribution of this Markov chain is the uniform distribution on X, i.e., the simulation begins with a random checkerboard of volume fraction ϕ. The transition probability matrix is defined such that x^{i_k} and $x^{i_{k+1}}$ differ by two neighboring points having their phases inverted. A move from state x^j to state $x^k (x^j, x^k \in X)$ satisfying the latter requirement is accepted with probability

$$p_i(x^j, x^k) = \min(1, \exp(-\Delta E_{jk}/T_i)), \tag{6}$$

where T_i is a "temperature" at time i,

$$\Delta E_{jk} = E(x^k) - E(x^j) \tag{7}$$

is the change in fictitious energy of the configuration when going from x^j to x^k. We define the fictitious energy $E(\cdot)$ as the square of the difference between the NMR signal of the current configuration $TM(\mathbf{k}_m; x^j)$ and the target configuration $TM(\mathbf{k}_m)$, summed over all wave vectors in the experiment:

$$E(x^j) = \frac{1}{n_k}\sum_{\mathbf{k}_m \in K}[TM(\mathbf{k}_m) - TM(\mathbf{k}_m; x^j)]^2, \tag{8}$$

where $K = \{\mathbf{k}_1, \mathbf{k}_2, \ldots, \mathbf{k}_{n_k}\}$.

In addition to flipping only pairs of neighboring points, the second departure from Kirkpatrick's algorithm aimed at speeding up convergence consists of starting with a coarse grid of 8^3. The configuration is evolved until an apparent plateau in the configuration energy is reached, i.e., until convergence reaches a much slower rate, at which point the grid size is increased to 16^3. Evolution proceeds, then a final pass is done on a 32^3 grid. The steps are summarized in Algorithm 1 (Fig. 2).

The temperature cooling schedule employed consisted of monitoring the acceptance rate every 20 moves, by looking at the past group of 20 moves and decreasing the temperature by a factor of 5 if more than 10% of the last 20 moves had been accepted. If, on the other hand, more than 30 consecutive moves had been rejected, the temperature would be increased by a factor of 1.5. A jump was made from coarse matrix to the next finer matrix according to whether the energy appeared to have reached a local minimum. These transition times were nearly the same for all simulations. Unlike the inverse logarithmic ($C/\ln t$) schedule [7], convergence using this approach is not guaranteed but at least gives reasonable computation times.

1.3. Signal as function of correlation distance

We use the method of fast Fourier transformation (FFT) [8] to calculate the magnetic dipolar interactions on a cartesian grid. This permits speedy calculations of the dipolar field for a given configuration of the indicator function. The signal intensity is calculated from a discrete version of Eq. (A.15):

$$T_i(\mathbf{k}_m) = \sum_{\mathbf{r}_l \in U} M_j(\mathbf{r}_l)B_k(\mathbf{r}_l) - M_k(\mathbf{r}_l)B_j(\mathbf{r}_l), \tag{9}$$

where i,j,k are the three components of the magnetization along the usual basis (x,y,z), respectively, and cyclic permutations. This is essentially the same as Eq. (2), but applies to more general preparations than $90^\circ_x - 90^\circ_x$, provided the proper initial conditions are used as input. The dipolar field $\mathbf{B}(\mathbf{r})$ is calculated in Fourier space by numerical FFT of the magnetization $\mathbf{M}(\mathbf{r}) \rightarrow \tilde{\mathbf{M}}(\mathbf{k})$ and use of a formula given by Deville [9] (and derived in Appendix B).

We pick a number of wave vectors $\mathbf{k}_m \in \{\mathbf{k}_1, \mathbf{k}_2, \ldots, \mathbf{k}_{n_k}\}$, by adjusting the gradient area and direction. We found a good compromise between reconstruction accuracy and computation time by using $\lambda_m = 2\pi/k_m$ of 10, 16, and 32 points for the 32^3 grid and three orthogonal gradient directions (x,y,z) so that $n_k = 9$. The dipolar field essentially encodes the geometry of the sample's fluid

choose target geometry, one of: sphere, cylinder (horizontal or vertical), phase-inverted sphere, phase-inverted cylinder
generate target geometry on 32^3 grid with volume fraction ϕ for the liquid phase
calculate target signal $TM(\mathbf{k}_m)$ for all 9 values of $\mathbf{k}_m$
$t = 0$
for grid sizes $N_i = 8, 16$ and 32 (in increasing order) **do**
  if $N_i = 8$ **then**
    generate random checkerboard with volume fraction ϕ on grid of size 8^3
  else
    move on to next grid size $N_i \rightarrow N_{i+1}$
  end if
  while $E(x_{i_t}) \geq E_{thresh}(N_i)$ **do**
    $t = t + 1$
    invert phase of a pair of neighboring points chosen at random (with uniform distribution)
    calculate NMR signal of the new configuration (see Algorithm 2)
    calculate $E(x^{i_t})$, the energy of the new configuration (last step of Algorithm 2)
    pick random number $r \in [0, 1]$ uniformly
    if $r \geq \min(1, \exp(-\Delta E_{i_t, i_{t-1}}/T_t))$ where $\Delta E_{i_t, i_{t-1}} = E(x^{i_t}) - E(x^{i_{t-1}})$ **then**
      reject move (return to $t = t - 1$)
      keep old configuration $x^{i_{t-1}}$
      keep old energy $E(x^{i_{t-1}})$
    else
      accept new configuration x^{i_t}
      accept new energy $E(x^{i_t})$
    end if
    temperature T_t is decreased if required
  end while
  if $N_i = 32$ **then**
    end of simulation
  end if
end for

Fig. 2. Evolution of the indicator function (Algorithm 1).

phase over a distance scale that is determined by the wave number $k_m = |\mathbf{k}_m|$ and the direction of the vector $\mathbf{k}_m$.

The simulation and FFT operations are all done on the 32^3 grid. Simulations at smaller grid sizes 8^3 and 16^3 are done on the 32^3 grid by manipulating larger clusters of points as needed. For each grid size N_i, a threshold energy $E_{\text{thresh}}(N_i)$ where convergence had reached a much slower rate was used to move on to the next grid size $N_i \rightarrow N_{i+1}$. The transition to higher grid sizes $N_1 \rightarrow N_2 \rightarrow N_3$ is done by moving smaller clusters of points. To reduce the effect of ghost cells in the FFT, the phase space X was further restricted to ensure there was a minimum of 4 pixels at the edge of the 32^3 grid where the indicator function is identically 0. The calculation of signal intensities is summarized in Algorithm 2 (Fig. 3).

1.4. Markers of structural anisotropy

For a broad class of materials, the degree of structural anisotropy is important. For example, in materials where mechanical properties are of interest, structural anisotropy tensors based on measurements of the mean intercept length in orthotropic materials can be related to the elastic moduli [10]. The lower-order statistical descriptors that are of interest in characterizing random media (such as the lineal path function, and n-point correlation functions [11]) can, in theory, be obtained from the reconstruction. We recall that the n-point correlation function for the liquid phase is given by the classical ensemble average,

$$S_n(\mathbf{x}_1, \ldots, \mathbf{x}_n) = \langle \chi_U(\mathbf{x}_1) \ldots \chi_U(\mathbf{x}_n) \rangle = \int_\Omega \chi_{U(\omega)}(\mathbf{x}_1) \ldots \chi_{U(\omega)}(\mathbf{x}_n) \mathsf{P}(\mathrm{d}\omega), \quad (10)$$

where the average is computed over a large number of realizations of the random medium in order to represent the joint probability $\mathsf{P}\{\chi_U(\mathbf{x}_1) = 1; \ldots; \chi_U(\mathbf{x}_n) = 1\}$. The 2-point correlation function is given by:

$$S_2(\mathbf{x}_1, \mathbf{x}_2) = \langle \chi_U(\mathbf{x}_1) \chi_U(\mathbf{x}_2) \rangle = \int_\Omega \chi_{U(\omega)}(\mathbf{x}_1) \chi_{U(\omega)}(\mathbf{x}_2) \mathsf{P}(\mathrm{d}\omega). \quad (11)$$

To quantify material anisotropy, this correlation function can be calculated along any specific direction; any dependence on orientation of the line adjoining

1: **for** all $\mathbf{k}_m \in \{\mathbf{k}_1, \mathbf{k}_2, \ldots, \mathbf{k}_{n_k}\}$ **do**
2: calculate $\mathbf{M}(\mathbf{r}_i)$ on a 32^3 grid, $\mathbf{r}_i \in U$ for the CRAZED preparation (Figure 1) with a given value of $\mathbf{k}_m$ for current configuration x^{i_t}
3: FFT of magnetization distribution: $\mathbf{M}(\mathbf{r}_i) \to \tilde{\mathbf{M}}(\mathbf{k}_i)$
4: calculate dipolar field

$$\tilde{\mathbf{B}}(\mathbf{k}_i) = \frac{4\pi}{6}\left[3\tilde{M}_z(\mathbf{k}_i)\hat{\mathbf{z}} - \tilde{\mathbf{M}}(\mathbf{k}_i)\right]\left[1 - 3(\hat{\mathbf{k}}_i \bullet \hat{\mathbf{z}})^2\right]$$

where $\mathbf{k}_i$ runs over the entire grid and $\hat{\mathbf{k}}_i$ is the unit vector $\mathbf{k}_i/|\mathbf{k}_i|$.
5: inverse FFT: $\tilde{\mathbf{B}}(\mathbf{k}_i) \to \mathbf{B}(\mathbf{r}_i)$
6: calculate total x and y components of the NMR signal $T_x(\mathbf{k}_m)$ and $T_y(\mathbf{k}_m)$ using

$$T_i(\mathbf{k}_m) = \sum_{\mathbf{r}_l \in U} M_j(\mathbf{r}_l)B_k(\mathbf{r}_l) - M_k(\mathbf{r}_l)B_j(\mathbf{r}_l)$$

where $(i, j, k) = (x, y, z)$ and cyclic permutations
7: **end for**
8: calculate energy of the configuration $E(x^{i_t})$ and the set of numbers:

$$TM(\mathbf{k}_m) = \left[T_x^2(\mathbf{k}_m) + T_y^2(\mathbf{k}_m)\right]^{1/2}, m = 1, \ldots, n_k$$

Fig. 3. Calculation of NMR signal (Algorithm 2).

the 2 points will reflect the degree of anisotropy. Since there are not enough realizations in this study to compute ensemble averages, we instead assume statistical homogeneity, so that the 2-point correlation function depends only on the distance $r = |\mathbf{x}_1 - \mathbf{x}_2|$, and ergodicity [11] and replicate the 32^3 grid in a periodic array. S_2 is computed along the 3 principal axes by randomly tossing pairs of points $\mathbf{x}, \mathbf{x} + r\mathbf{e}_i \in U \cup V$ (with uniform distribution) over the array and counting the number of times both points fall simultaneously in the liquid phase to get the following three quantities:

$$\begin{aligned} S_x(r) &= \langle \chi_U(\mathbf{x})\chi_U(\mathbf{x} + r\hat{\mathbf{x}})\rangle \\ S_y(r) &= \langle \chi_U(\mathbf{x})\chi_U(\mathbf{x} + r\hat{\mathbf{y}})\rangle \\ S_z(r) &= \langle \chi_U(\mathbf{x})\chi_U(\mathbf{x} + r\hat{\mathbf{z}})\rangle \end{aligned} \tag{12}$$

A fully isotropic material has $S_x(r) = S_y(r) = S_z(r)$. For anisotropic media, the triple $(1/\phi)(S_x(r_0), S_y(r_0), S_z(r_0))$ can provide a useful quantifier of anisotropy. The point r_0 should be chosen sufficiently far from 0 since $S_i(0) = \phi$, i.e., $S_x(0) = S_y(0) = S_z(0)$ all equal the volume fraction, and it should be smaller than the grid size to avoid asymptotic volume fraction weighting $S_i(r) \to \phi^2$ as $r \to \infty$ which is usually attained exponentially fast [11].

2. Results

The simulated algorithm was implemented in the C programming language on a 1.7 MHz Pentium IV personal computer with 1 GB memory and the FreeBSD 5.1 operating system. Roughly five days were required to achieve 100,000 steps in each of the simulations, which aimed at reconstructing the following objects centered on a 32^3 grid: a sphere of radius 11 points, horizontal and vertical cylinders 24 points in length and cross-section of radius 7 points, and phase-inverted sphere and cylinder of the same radii and length as the non-inverted geometries. The phase-inverted geometries have the solid and liquid phases inverted. In this case, the liquid phase constitutes the medium which lies outside rather than inside the sphere/cylinder boundary, yielding an inclusion rather than a pore.

Fig. 4 shows image (2D) projections for the reconstructed media (A–E) for the corresponding target geometries (F–J). These images are obtained by summing the indicator function χ_{ijk} along the third dimension k and plotting the resulting intensity in the i,j plane. From these projections, it is clear that the algorithm can reconstruct and differentiate horizontal versus vertical cylinders. The reconstruction of the sphere appears slightly rectangular but the indicator function essentially covers the same volume and appears to preserve a good degree of isotropy. Phase-inverted geometries result in the liquid phase located mainly on the edges of the grid, with minimal liquid at the center of the grid. The phase-inverted cylinder contains far less liquid along the center of the projection than the phase-inverted sphere, as expected.

Because these summations along the third dimension do not reveal the full structure, it is helpful to plot 1D profiles along various dimensions. Figs. 5–9 show projections of the indicator function along various dimensions obtained, for example, by summing the first and second dimensions (i,j) of χ_{ijk} and plotting the sum along the third dimension k in the case of a 2-sphere

$$S^2(\mathbb{Z}) = \{(i,j,k) \in \mathbb{Z}^3 : (i - i_0)^2 + (j - j_0)^2 + (k - k_0)^2 \leqslant r^2\}$$

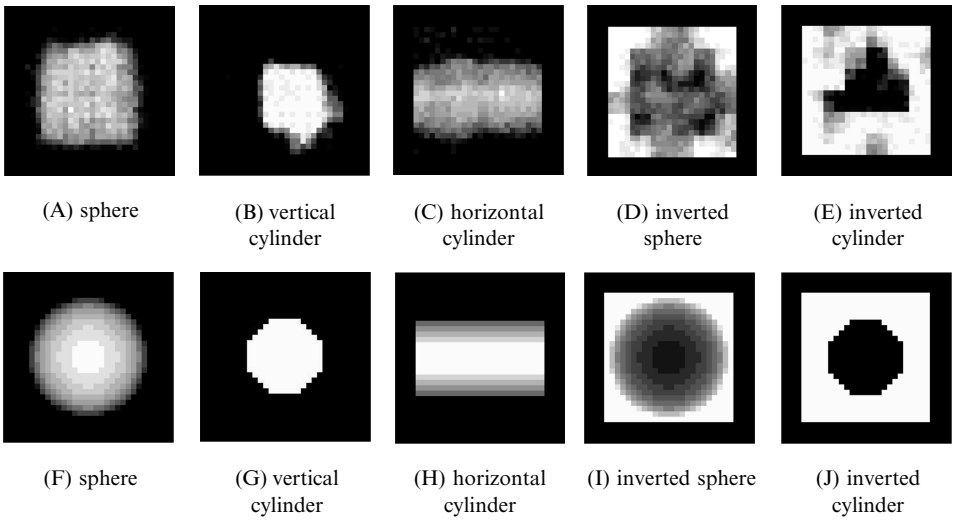

Fig. 4. Summations along k (third dimension) of the indicator function ($\sum_k \chi_{ijk}$) plotted as 2D images (intensity plots) for the various geometries. Frames (A–E) are for the reconstruction and frames (F–J) are for the target geometry.

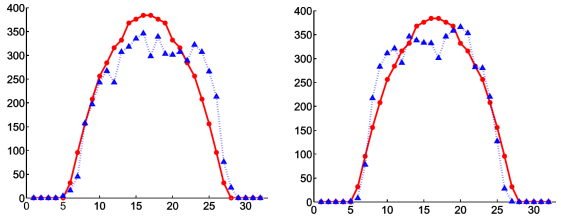

Fig. 5. Sphere geometry (●, target configuration; ▲, reconstruction). Summation of the matrix χ_{ijk} over the indices (A) i,j and (B) j,k as function of k and i, respectively.

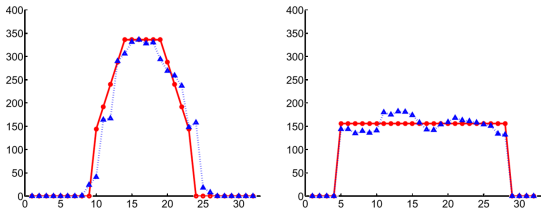

Fig. 7. Cylinder geometry (●, target configuration; ▲, reconstruction) with cylinder aligned along x (or i index). Summation of the matrix χ_{jk} over the indices (A) i,j and (b) j,k as function of k and i, respectively.

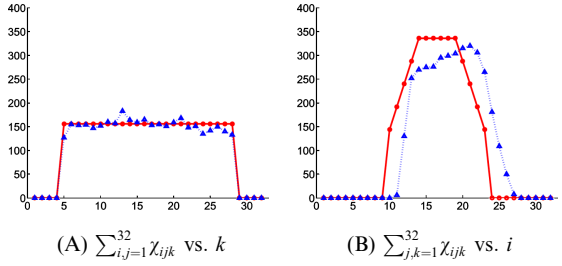

Fig. 6. Cylinder geometry (●, target configuration; ▲, reconstruction) with cylinder aligned along z (or k index). Summation of the matrix χ_{ijk} over the indices (A) i,j and (B) j,k as function of k and i, respectively.

produces a profile along k of the form

$$f(k) = \pi r^2 - \pi(k - k_0)^2, \tag{13}$$

and by symmetry, the same profile is expected along i and j. The i and k profiles are shown in Figs. 5A and B by the curves with round symbols (●), where $r = 11$ and $k_0 = 16$. The j profile (not shown) is similar to the i and k profiles.

Figs. 5–9 are plots generated using the reconstructed indicator function for a single simulation. The deviations between reconstructed (▲) and ideal (●) geometries in these plots are representative of typical errors obtained in a run of 100,000 steps.

The curves with triangular (▲) symbols in Fig. 5 are for the reconstruction of the spherical geometry (liquid-filled sphere). The largest deviations from the target profile are usually observed near the center of the sphere. The intrinsic noisiness of the stochastic reconstruction procedure, under the constraint of a fixed volume fraction, inevitably redistributes small amounts of the liquid phase away from the center. We also notice the nearly quadratic fall-off on opposite sides of the graphs.

The results of Fig. 6 are for the cylindrical geometry (liquid-filled cylinder) with the principal axis of the cylinder aligned along the z axis (k index). The rectangular profile is clearly depicted in Fig. 6A, where the stochastic reconstruction has produced only slightly rounded edges. We note that the transverse profile (Fig. 6B) approximates the circular cross-section albeit a small overall shift to the right of a few grid points. Such overall shifts may arise randomly but usually span no more than a few grid points. For this cylinder, the profile of the target configuration is of the form

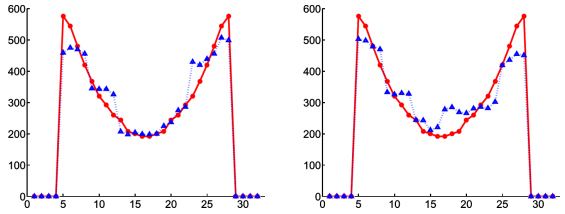

(A) $\sum_{i,j=1}^{32}\chi_{ijk}$ vs. k (B) $\sum_{j,k=1}^{32}\chi_{ijk}$ vs. i

Fig. 8. Phase-inverted sphere geometry (●, target configuration; ▲, reconstruction). Summation of the matrix χ_{ijk} over the indices (A) i,j and (B) j,k as function of k and i, respectively.

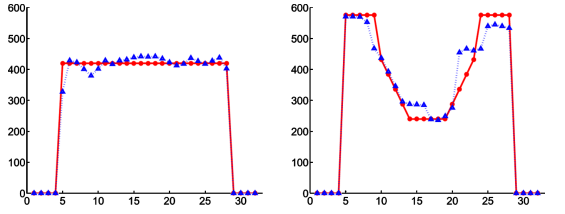

(A) $\sum_{i,j=1}^{32}\chi_{ijk}$ vs. k (B) $\sum_{i,k=1}^{32}\chi_{ijk}$ vs. j

Fig. 9. Phase-inverted cylinder geometry (●, target configuration; ▲, reconstruction). Summation of the matrix χ_{ijk} over the indices (A) i,j and (B) i,k as function of k and j, respectively.

$$f(i) = 2l(r^2 - (i - i_0)^2)^{1/2}, \tag{14}$$

where $r = 7$ is the cylinder radius, $i_0 = 16$ and $l = 24$ is its length. It is clear from these results that the algorithm can differentiate spherical from cylindrical pores.

In Fig. 7 the reconstruction was performed using the same cylindrical geometry, but for a cylindrical pore aligned horizontally instead of vertically. We conclude that the algorithm can correctly resolve the orientation of this cylinder.

The profiles of a phase-inverted sphere are illustrated in Figs. 8A and B by the curve with circular (●) symbols. The reconstruction (▲) is able to place the liquid phase on the outside, while minimizing the amount of liquid at the center of the grid.

Similar results for the phase-inverted cylinder show a good rectangular profile in Fig. 9A and more liquid on the edges of the grid than on the inside for the circular cross-section in Fig. 9B. We note that in Figs. 4, 8, and 9 there are 4 points at the edges of the grid which take the value 0. This is due to the restriction imposed on the phase space X (see last paragraph of Section 1.3).

Values of the 2-point correlation function evaluated at $r_0 = 8$ grid points are shown in Table 1. First we note excellent agreement between the values for the ideal/target geometries and the reconstructed medium, which confirms the ability of the algorithm to resolve coarse geometric features. The higher value for $S_z(r_0)$ in the case of the vertical cylinder and phase-inverted cylinder is indicative of structural anisotropy and results because

Table 1
Value of the 2-point correlation function evaluated at $r_0 = 8$

	Target geometry			Reconstruction		
	$S_x(r_0)$	$S_y(r_0)$	$S_z(r_0)$	$S_x(r_0)$	$S_y(r_0)$	$S_z(r_0)$
Sphere	0.10	0.10	0.10	0.10	0.10	0.10
Vertical cyl.	0.05	0.05	0.09	0.05	0.05	0.08
Horizontal cyl.	0.09	0.05	0.05	0.08	0.05	0.05
Inverted sphere	0.12	0.12	0.12	0.12	0.12	0.12
Inverted cyl.	0.15	0.15	0.24	0.15	0.15	0.23

the long axis of the cylinder is oriented along z. We also notice the higher value of 0.08 for $S_x(r_0)$ for the long axis of the cylinder in the case of the horizontal cylinder. Comparison to the vertical cylinder, where the value 0.08 occurs for $S_z(r_0)$ instead of $S_x(r_0)$ confirms that the 2-point correlation function can resolve the orientation of a cylinder. In this manner, markers of structural anisotropy can be obtained from triples $(S_x(r_0), S_y(r_0), S_z(r_0))$ which are in the form of a vector.

3. Discussion

3.1. Choice of grid size

In the example given above, the 2-point correlation function was calculated from the reconstructed data. There are much more efficient ways to compute this correlation function (see [1,4,12] for a direct method without the need for inversion). An important advantage of the reconstruction is that it allows, in principle, any other statistical descriptors of the geometry to be computed; see [11] for a comprehensive list of known descriptors. The fundamental limit in all cases is the accuracy of the reconstruction. It is anticipated that a larger sampling of k-space would improve the performance of the algorithm. However, more data points increase the computational load, which severely limits the grid size that can be used. Fig. 10 shows the progress of a typical simulation near the completion of each stage at 8^3, 16^3, and 32^3 grid sizes, after 1, 3, and 5 days of total computation time, respectively. The changes in going from 8^3 to 16^3 are substantial, however, in going to 32^3, the improvements are relatively small. For the objects in this study, a 16^3 grid would be enough to reproduce the shape reasonably well. All of our reconstructions were able to converge to the correct shape. For more complicated objects, such as 2 thin cylinders, or 2 spheres side-by-side, the reconstructions were less successful, sometimes converging to the correct shape, sometimes not. In these cases, the 8^3 grid is generally too coarse a starting point to provide an adequate phase space required to the search algorithm, while the 16^3 random checkerboard converges too slowly.

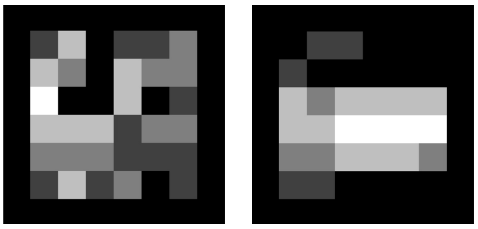

(A) $8\times8\times8$ at $t=0$ (B) $8\times8\times8$ at $t=1$ day

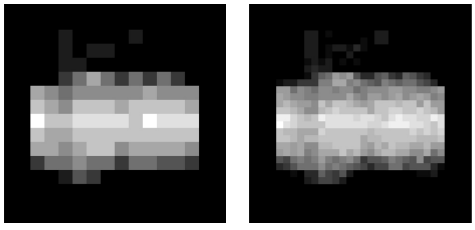

(C) $16\times16\times16$ at $t=3$ days (D) $32\times32\times32$ at $t=5$ days

Fig. 10. Summations along k of the indicator function χ_{ijk} plotted as 2D images for the horizontal cylinder, at different stages and grid sizes in the simulation.

3.2. log N speed improvement

Complete convergence in this study was not attained, due to the high computational costs. Most of the time is spent calculating the dipolar field (an $O(N^3 \log N)$ operation) for several CRAZED preparations of different wave vectors. Direct calculations of a double volume integral such as formula (2) would require $O(N^6)$ operations, which is even less efficient. A careful look at such calculations reveals that $T(\mathbf{k})$ varies only by a small amount when pairs of points are flipped. In this section, we show that a perturbative expansion of the double integral in terms of functional derivatives is possible and results in a $O(N^3)$ method. When regarding $\mathbf{k}$ as a parameter, double integrals such as Eq. (2) can be expressed as a functional of the indicator function $\chi(\mathbf{r})$:

$$T[\chi] = \int\int \chi(\mathbf{r})\chi(\mathbf{r}')f(\mathbf{r},\mathbf{r}')\,\mathrm{d}^3\mathbf{r}'\,\mathrm{d}^3\mathbf{r}. \tag{15}$$

In the case of Eq. (2) the kernel is $f(\mathbf{r},\mathbf{r}') = K(\mathbf{r},\mathbf{r}')\cos(\mathbf{k}\cdot\mathbf{r})\,[\sin(\mathbf{k}\cdot\mathbf{r}') - \sin(3\,\mathbf{k}\cdot\mathbf{r}')]$. The simulated annealing move produces a change $\Delta\chi$ in the indicator function χ, which is expressed as a transformation: $\chi \to \chi + \Delta\chi$. In the present case, $\Delta\chi$ is the flipping of pairs of points; we may expand the functional as a Taylor series to first order in the perturbation function $\Delta\chi$ (see, for example, [13] or [14]):

$$T[\chi+\Delta\chi] = T[\chi] + \int_{\mathbb{R}^3} \frac{\delta T}{\delta\chi(\mathbf{r})}\Delta\chi(\mathbf{r})\,\mathrm{d}^3\mathbf{r} + o[\Delta\chi], \tag{16}$$

where, given any $\epsilon > 0$, there exists $\delta > 0$ such that $o[\Delta\chi] < \epsilon\cdot\sup|\Delta\chi|$ holds for any choice of $\Delta\chi(\cdot)$, whenever $\sup|\Delta\chi| < \delta$. The functional derivative $\frac{\delta T}{\delta\chi(\mathbf{r})}$ is the limit:

$$\begin{aligned}\frac{\delta T}{\delta\chi(\mathbf{r})} &= \lim_{\epsilon\to0}\frac{1}{\epsilon}\left\{\int\int [\chi(\mathbf{r}'') + \epsilon\delta(\mathbf{r}''-\mathbf{r})][\chi(\mathbf{r}') \right.\\ &\quad + \epsilon\cdot\delta(\mathbf{r}'-\mathbf{r})]f(\mathbf{r}'',\mathbf{r}')\,\mathrm{d}^3\mathbf{r}''\,\mathrm{d}^3\mathbf{r}'\\ &\quad \left. - \int\int \chi(\mathbf{r}'')\chi(\mathbf{r}')f(\mathbf{r}'',\mathbf{r}')\,\mathrm{d}^3\mathbf{r}''\,\mathrm{d}^3\mathbf{r}'\right\}\\ &= \int\int [\delta(\mathbf{r}''-\mathbf{r})\chi(\mathbf{r}')f(\mathbf{r}'',\mathbf{r}')\\ &\quad + \chi(\mathbf{r}'')\delta(\mathbf{r}'-\mathbf{r})f(\mathbf{r}'',\mathbf{r}')]\,\mathrm{d}^3\mathbf{r}''\,\mathrm{d}^3\mathbf{r}'\\ &= \int \mathrm{d}^3\mathbf{r}'\chi(\mathbf{r}')[f(\mathbf{r},\mathbf{r}') + f(\mathbf{r}',\mathbf{r})]\end{aligned} \tag{17}$$

On a 3D grid of points $\mathscr{G}$ this is calculated as a sum ($O(N^3)$ operations):

$$\int \mathrm{d}^3\mathbf{r}'\chi(\mathbf{r}')[f(\mathbf{r},\mathbf{r}') + f(\mathbf{r}',\mathbf{r})] \sim \sum_{r_i\in\mathscr{G}} \chi_{r_i}[f_{r,r_i} + f_{r_i,r}] \tag{18}$$

The Taylor expansion becomes:

$$T[\chi+\Delta\chi] \sim T[\chi] + \sum_{r_1\in\mathscr{G}}\sum_{r_2\in\mathscr{G}} \chi_{r_2}[f_{r_1,r_2} + f_{r_2,r_1}]\Delta\chi_{r_1} \tag{19}$$

In the simple case where the phases of points $\bar{r}_1$ and $\bar{r}_2$ are reversed, the perturbation has the form:

$$\Delta\chi_r = \Delta^+(r-\bar{r}_1) + \Delta^-(r-\bar{r}_2), \tag{20}$$

where $\Delta^\pm(r-\bar{r}_1) = \pm1$ whenever $r = \bar{r}_1$ and 0 otherwise. Thus,

$$\begin{aligned}T[\chi+\Delta\chi] &\sim T[\chi] + \sum_{r_1\in\mathscr{G}}\sum_{r_2\in\mathscr{G}} \chi_{r_2}(f_{r_1,r_2} + f_{r_2,r_1})\\ &\quad\cdot[\Delta^+(r_1-\bar{r}_1) + \Delta^-(r_1-\bar{r}_2)]\\ &= T[\chi] + \sum_{r_i\in\mathscr{G}} \chi_{r_i}[f_{\bar{r}_1,r_i} + f_{r_i,\bar{r}_1} - f_{\bar{r}_2,r_i} - f_{r_i,\bar{r}_2}]\end{aligned} \tag{21}$$

which says that the signal intensity as function of correlation distance, for a modified indicator function $\chi + \Delta\chi$ equals the old one $T[\chi]$, plus a correction term $\sum_{r_i\in\mathscr{G}}\chi_{r_i}[f_{\bar{r}_1,r_i} + f_{r_i,\bar{r}_1} - f_{\bar{r}_2,r_i} - f_{r_i,\bar{r}_2}]$. This correction term is $O(N^3)$.

3.3. Extension to multiphase materials

In a manner analogous to the annealing algorithms which aim at reconstructing multiphase random media from any number and types of correlation functions (see, for example, [15–17]), the present algorithm can easily be extended to handle several magnetization components of different magnetization densities and susceptibility. To accomplish this, it would be necessary to assume knowledge of the volume fraction, magnetization density, and susceptibility for each component; these would be held constant during the simulation. A set of indicator functions, one for each phase, would be required along with the flipping of pairs of points between any two randomly chosen phases of the medium. Since the induced magnetic fields are sums over all the

dipoles in the medium, the calculation amounts to a DDF calculation for all the different phases.

3.4. Gas phase measurements

Other NMR techniques exist for probing porous material structure. NMR diffusion and relaxation methods can effectively probe micron-scale pores [18] but diffusion in liquids is too slow to probe larger scales. MRI allows larger pores to be spatially resolved but SNR limitations often hamper its use as a microscopy tool. More recently, a promising new technique using ^{129}Xe gas phase measurements has been shown to be useful over intermediate scales (100–2000 μm) [19]. With the exception of MRI, current techniques generally do not provide the indicator function of the pores. Methods based on the DDF can directly probe the indicator function using NMR signal from the fluid phase, without the need to introduce probing agents or any specific modeling of the data. If the pores of a material are empty, a drawback is that a fluid needs to be introduced; however, the penetration of fluid inside small pores is not as good as that of inert gas. Also, because it does not rely on relaxation mechanisms, the DDF method cannot probe surface properties. Consequently, nuclei which relax by quadrupolar interactions such as ^{131}Xe may be more useful [20].

4. Conclusion

We have demonstrated in theory that three-dimensional indicator functions for the geometry of a biphasic material, whose liquid phase is observable by NMR and its solid phase does not contribute to the signal, can be obtained through numerical inversion by simulated annealing of an integral equation which describes the NMR signal as function of material geometry and pulse sequence parameters. The main finding of this research is that a simple cost function, which aims at matching the signal dependence of a CRAZED sequence with correlation gradient strength and direction to the signal dependence of the target geometry, proved sufficient to reconstruct basic spherical and cylindrical geometries on a 32^3 grid using as little as 3 different gradient strengths and 3 orthogonal directions. We have chosen the CRAZED experiment because it is based on volume measurements of the distant dipolar field, which encode the material geometry over various length scales. This provides a method for directly probing the geometry of porous materials by NMR in cases where high-resolution imaging is not an option, or in cases where the structures are too large to be resolved by diffusion-based methods. While in the present study, the simulation looks at the NMR signal of the entire sample, this could just as easily be the spatially resolved signal from a single pixel. Hence, it could be used for the spatial mapping of coarse geometric quantifiers. We have demonstrated its application to calculating a marker of anisotropy using the reconstructed medium.

Acknowledgments

This work was funded by NIH Grant EB2122. We thank professor Marcel Utz of the physics department of the University of Connecticut for drawing our attention to [17], which led to the idea proposing the use of a perturbation expansion.

Appendix A. Integral equation for the signal

In this Appendix we derive an expression for the dependence of the signal intensity at the conclusion of the double-quantum CRAZED preparation of Fig. 1. Two gradient pulses are applied with the same polarity.

For simplicity, we neglect relaxation and diffusion because these mechanisms do not contribute to the structural dependence of the signal intensity we wish to investigate. The results hold for short evolution times, where only a small amount of non-linear evolution takes place. Extension to longer evolution times or strong dipolar fields is straightforward but not practical because a Taylor expansion in time of the magnetization evolution requires a large number of terms.

A.1. Simple iDQC CRAZED preparation

We denote the initial magnetization as $(0,0,M_z)$, where $M_z = \chi_U(\mathbf{r})M_0^U + \chi_V(\mathbf{r})M_0^V$, M_0^U is the equilibrium magnetization of the liquid phase, M_0^V is the equilibrium magnetization for the solid phase. We consider media for which $M_0^V = 0$ and simply write $M_0^U = M_0$ for short and we consider a simple iDQC CRAZED sequence for short evolution times τ, where evolution under the DDF is negligible. A clockwise rotation of angle α about the x axis of the initial magnetization gives:

$$\begin{aligned} M_x(\mathbf{r}) &= 0, \\ M_y(\mathbf{r}) &= \chi_U(\mathbf{r})M_0 \sin\alpha, \\ M_z(\mathbf{r}) &= \chi_U(\mathbf{r})M_0 \cos\alpha. \end{aligned} \tag{A.1}$$

The first gradient pulse whose direction and area defines a wave vector $\mathbf{k}$ turns this into a spatially dependent sinusoid modulation. For a local resonance frequency offset $\delta_\mathbf{r} = \Delta\omega(\mathbf{r})$ we have:

$$\begin{aligned} M_x(\mathbf{r}) &= -\chi_U(\mathbf{r})M_0 \sin\alpha \sin(\mathbf{k}\cdot\mathbf{r} + \delta_\mathbf{r}\tau), \\ M_y(\mathbf{r}) &= \chi_U(\mathbf{r})M_0 \sin\alpha \cos(\mathbf{k}\cdot\mathbf{r} + \delta_\mathbf{r}\tau), \\ M_z(\mathbf{r}) &= \chi_U(\mathbf{r})M_0 \cos\alpha. \end{aligned} \tag{A.2}$$

The second rf pulse (β) induces a clockwise rotation:

$$
\begin{aligned}
M_x(\mathbf{r}) &= -\chi_U(\mathbf{r})M_0 \sin\alpha \sin(\mathbf{k}\cdot\mathbf{r}+\delta_{\mathbf{r}}\tau),\\
M_y(\mathbf{r}) &= \chi_U(\mathbf{r})M_0(\sin\alpha\cos\beta\cos(\mathbf{k}\cdot\mathbf{r}+\delta_{\mathbf{r}}\tau)+\cos\alpha\sin\beta),\\
M_z(\mathbf{r}) &= \chi_U(\mathbf{r})M_0(-\sin\alpha\sin\beta\cos(\mathbf{k}\cdot\mathbf{r}+\delta_{\mathbf{r}}\tau)+\cos\alpha\cos\beta).
\end{aligned}
\tag{A.3}
$$

Then applying the second gradient pulse $\mathbf{k}'$ to produce a counter-clockwise rotation of angle $\mathbf{k}'\cdot\mathbf{r}+2\delta_{\mathbf{r}}\tau$:

$$
\begin{aligned}
M_x(\mathbf{r}) &= \chi_U(\mathbf{r})M_0[-\sin\alpha\sin(\mathbf{k}\cdot\mathbf{r}+\delta_{\mathbf{r}}\tau)\cos(\mathbf{k}'\cdot\mathbf{r}+2\delta_{\mathbf{r}}\tau)\\
&\quad -\sin\alpha\cos\beta\sin(\mathbf{k}'\cdot\mathbf{r}+2\delta_{\mathbf{r}}\tau)\cos(\mathbf{k}\cdot\mathbf{r}+\delta_{\mathbf{r}}\tau)\\
&\quad -\sin\beta\cos\alpha\sin(\mathbf{k}'\cdot\mathbf{r}+2\delta_{\mathbf{r}}\tau)],\\
M_y(\mathbf{r}) &= \chi_U(\mathbf{r})M_0[-\sin\alpha\sin(\mathbf{k}\cdot\mathbf{r}+\delta_{\mathbf{r}}\tau)\sin(\mathbf{k}'\cdot\mathbf{r}+2\delta_{\mathbf{r}}\tau)\\
&\quad +\sin\alpha\cos\beta\cos(\mathbf{k}'\cdot\mathbf{r}+2\delta_{\mathbf{r}}\tau)\cos(\mathbf{k}\cdot\mathbf{r}+\delta_{\mathbf{r}}\tau)\\
&\quad +\sin\beta\cos\alpha\cos(\mathbf{k}'\cdot\mathbf{r}+2\delta_{\mathbf{r}}\tau)],\\
M_z(\mathbf{r}) &= \chi_U(\mathbf{r})[M_0(-\sin\alpha\sin\beta\cos(\mathbf{k}\cdot\mathbf{r}+\delta_{\mathbf{r}}\tau)\\
&\quad +\cos\alpha\cos\beta)].
\end{aligned}
\tag{A.4}
$$

Taking $\alpha=\beta=90^\circ$ gives $\cos\alpha=\cos\ \beta=0$, $\sin\ \alpha=\sin\ \beta=1$ and the expression simplifies to:

$$
\begin{aligned}
M_x(\mathbf{r}) &= -\chi_U(\mathbf{r})M_0\sin(\mathbf{k}\cdot\mathbf{r}+\delta_{\mathbf{r}}\tau)\cos(\mathbf{k}'\cdot\mathbf{r}+2\delta_{\mathbf{r}}\tau),\\
M_y(\mathbf{r}) &= -\chi_U(\mathbf{r})M_0\sin(\mathbf{k}\cdot\mathbf{r}+\delta_{\mathbf{r}}\tau)\cos(\mathbf{k}'\cdot\mathbf{r}+2\delta_{\mathbf{r}}\tau),\\
M_z(\mathbf{r}) &= -\chi_U(\mathbf{r})M_0\cos(\mathbf{k}\cdot\mathbf{r}+\delta_{\mathbf{r}}\tau)
\end{aligned}
\tag{A.5}
$$

and this is equivalent to:

$$
\begin{aligned}
M_x(\mathbf{r}) &= -\chi_U(\mathbf{r})(M_0/2)(\sin(\mathbf{r}\cdot(\mathbf{k}+\mathbf{k}')+3\delta_{\mathbf{r}}\tau)\\
&\quad +\sin(\mathbf{r}\cdot(\mathbf{k}-\mathbf{k}')-\delta_{\mathbf{r}}\tau)),\\
M_y(\mathbf{r}) &= \chi_U(\mathbf{r})(M_0/2)(\cos(\mathbf{r}\cdot(\mathbf{k}+\mathbf{k}')+3\delta_{\mathbf{r}}\tau)\\
&\quad -\cos(\mathbf{r}\cdot(\mathbf{k}-\mathbf{k}')-\delta_{\mathbf{r}}\tau)),\\
M_z(\mathbf{r}) &= -\chi_U(\mathbf{r})M_0\cos(\mathbf{k}\cdot\mathbf{r}+\delta_{\mathbf{r}}\tau).
\end{aligned}
\tag{A.6}
$$

In the case of where the gradients are in a 2:1 ratio ($\mathbf{k}'=2\mathbf{k}$), we substitute $\mathbf{k}'-\mathbf{k}=\mathbf{k}$ and $\mathbf{k}'+\mathbf{k}=3\mathbf{k}$ and get:

$$
\begin{aligned}
M_x(\mathbf{r}) &= \chi_U(\mathbf{r})(M_0/2)(\sin(\mathbf{r}\cdot\mathbf{k}+\delta_{\mathbf{r}}\tau)\\
&\quad -\sin(3\mathbf{r}\cdot\mathbf{k}+3\delta_{\mathbf{r}}\tau)),\\
M_y(\mathbf{r}) &= \chi_U(\mathbf{r})(M_0/2)(\cos(3\mathbf{r}\cdot\mathbf{k}+3\delta_{\mathbf{r}}\tau)\\
&\quad -\cos(\mathbf{r}\cdot\mathbf{k}+\delta_{\mathbf{r}}\tau)),\\
M_z(\mathbf{r}) &= -\chi_U(\mathbf{r})M_0\cos(\mathbf{k}\cdot\mathbf{r}+\delta_{\mathbf{r}}\tau).
\end{aligned}
\tag{A.7}
$$

In the next section only, we denote this magnetization vector following a CRAZED preparation as $\mathbf{M}_0(\mathbf{r})=(M_x(\mathbf{r}),M_y(\mathbf{r}),M_z(\mathbf{r}))$, and we will use this as the initial ($t=0$) magnetization distribution for a given value of the equilibrium magnetization density M_0.

A.2. Equations of motion

The magnetization evolution $\mathbf{M}_0(\mathbf{r})\rightarrow\mathbf{M}_t(\mathbf{r})$ in the rotating frame is given by:

$$
\mathbf{M}_t(\mathbf{r}) = \mathbf{M}_0(\mathbf{r}) + \gamma\mathbf{M}_t(\mathbf{r})\times\mathbf{B}(\mathbf{r})t + \mathbf{o}(\mathbf{r},t),
\tag{A.8}
$$

where $\mathbf{B}(\mathbf{r})$ is the dipolar field acting on the magnetization at $\mathbf{r}$ at time $t=0$, and $\mathbf{o}(\mathbf{r},t)$ is a function with the property that $\lim_{t\rightarrow 0}\|\mathbf{o}(\mathbf{r},t)\|/|t|=0$. The time axis is as in Fig. 1. To get the bulk magnetization $\mathbf{T}_t$, we integrate over the liquid phase:

$$
\begin{aligned}
\mathbf{T}_t &= \int_{\mathbb{R}^3}\chi_U(\mathbf{r})\mathbf{M}_t(\mathbf{r})\,\mathrm{d}^3\mathbf{r} = \int_U \mathbf{M}_t(\mathbf{r})\,\mathrm{d}^3\mathbf{r}\\
&= \int_U \mathbf{M}_0(\mathbf{r})\,\mathrm{d}^3\mathbf{r} + \gamma t\int_U \mathbf{M}_0(\mathbf{r})\times\mathbf{B}(\mathbf{r})\,\mathrm{d}^3\mathbf{r} + \mathbf{o}(\mathbf{r},t).
\end{aligned}
\tag{A.9}
$$

The first term on the right hand side is zero after a CRAZED preparation, assuming that the gradient pulses act as perfect spoiler gradients:

$$
\mathbf{T}_t(\mathbf{k}) = \int_U \mathbf{M}_t(\mathbf{r})\,\mathrm{d}^3\mathbf{r} = \gamma t\int_U \mathbf{M}_0(\mathbf{r})\times\mathbf{B}(\mathbf{r})\,\mathrm{d}^3\mathbf{r} + \mathbf{o}(\mathbf{r},t)
\tag{A.10}
$$

we denote the total magnetization by $\mathbf{T}_t(\mathbf{k})$ since the magnetization has been modulated according to the wavevector $\mathbf{k}$.

A.3. Observed signal

The observed signal is the complex quantity $T_{t,x}+iT_{t,y}$. The ith component of this cross-product, where $(i,j,k)=(x,y,z)$ and cyclic permutations, is given by:

$$
T_{t,i}(\mathbf{k}) = \gamma t\int_U \left[M_j(\mathbf{r})B_k(\mathbf{r}) - M_k(\mathbf{r})B_j(\mathbf{r})\right]\mathrm{d}^3\mathbf{r},
\tag{A.11}
$$

where

$$
\begin{aligned}
B_{x,y}(\mathbf{r}) &= \frac{\mu_0}{4\pi}\int_U K(\mathbf{r},\mathbf{r}')M_{x,y}(\mathbf{r}')\,\mathrm{d}^3\mathbf{r}',\\
B_z(\mathbf{r}) &= \frac{\mu_0}{4\pi}\int_U K(\mathbf{r},\mathbf{r}')(-2M_z(\mathbf{r}'))\,\mathrm{d}^3\mathbf{r}'
\end{aligned}
\tag{A.12}
$$

and $K(\mathbf{r},\mathbf{r}')$ stands for $(3\cos^2\theta-1)/2|\mathbf{r}-\mathbf{r}'|^3$. Neglecting field inhomogeneities ($\delta_{\mathbf{r}}=0$), the initial magnetization is

$$
\begin{aligned}
M_x(\mathbf{r}) &= \chi_U(\mathbf{r})(M_0/2)(\sin\mathbf{r}\cdot\mathbf{k}-\sin 3\mathbf{r}\cdot\mathbf{k}),\\
M_y(\mathbf{r}) &= \chi_U(\mathbf{r})(M_0/2)(\cos 3\mathbf{r}\cdot\mathbf{k}-\cos\mathbf{r}\cdot\mathbf{k}),\\
M_z(\mathbf{r}) &= -\chi_U(\mathbf{r})M_0\cos(\mathbf{k}\cdot\mathbf{r}),
\end{aligned}
\tag{A.13}
$$

and we get, upon substitution:

$$
\begin{aligned}
T_{t,y}(\mathbf{k}) &= \frac{3}{8\pi}\mu_0\gamma M_0^2 t\int_U\int_U \mathrm{d}^3\mathbf{r}'\,\mathrm{d}^3\mathbf{r}\chi_U(\mathbf{r})\chi_U(\mathbf{r}')K(\mathbf{r},\mathbf{r}')\\
&\quad\times\cos(\mathbf{k}\cdot\mathbf{r})[\sin(\mathbf{k}\cdot\mathbf{r}')-\sin(3\mathbf{k}\cdot\mathbf{r}')].
\end{aligned}
\tag{A.14}
$$

The corresponding expression for $T_{t,x}(\mathbf{k})$ is obtained by substituting the two occurrences of sin for −cos. For the purpose of obtaining and comparing numerical solutions for various material geometries, we discard the constants and write $T_i(\mathbf{k})$ for integrals of the type:

$$
T_i(\mathbf{k}) = \int_U [M_j(\mathbf{r})B_k(\mathbf{r}) - M_k(\mathbf{r})B_j(\mathbf{r})]\,\mathrm{d}^3\mathbf{r}
\tag{A.15}
$$

and we take M and B to be dimensionless quantities for the numerical simulations.

Appendix B. Dipolar field in Fourier space

In this appendix we present a simple proof of the expression for the dipolar field in Fourier space (Deville et al. [9]). The part of the dipolar field which is invariant to rotations about the z-axis is given in real space by the formula:

$$\mathbf{B}(\mathbf{r}) = \int_{\mathbb{R}^3} \mathrm{d}^3\mathbf{r}' \frac{1-3\cos^2\theta}{2|\mathbf{r}-\mathbf{r}'|^3}[3M_z(\mathbf{r}')\hat{\mathbf{z}} - \mathbf{M}(\mathbf{r}')], \tag{B.1}$$

where $\cos\theta = \hat{\mathbf{z}}\cdot(\mathbf{r}-\mathbf{r}')/|\mathbf{r}-\mathbf{r}'|$. This is a convolution in real space of $M_i(\mathbf{r}')$ with $\varphi(\mathbf{r}') = (1-3\cos^2\theta)/2|\mathbf{r}-\mathbf{r}'|$. In Fourier space it is a multiplication of their respective Fourier transforms $\tilde{M}_i(\mathbf{k})$ and $\tilde{\varphi}(\mathbf{k})$:

$$\tilde{\mathbf{B}}(\mathbf{k}) = \frac{4\pi}{6}[3\tilde{M}_z(\mathbf{k})\hat{\mathbf{z}} - \tilde{\mathbf{M}}(\mathbf{k})][1-3(\hat{\mathbf{k}}\cdot\hat{\mathbf{z}})^2]. \tag{B.2}$$

This is proved by doing the change of variables $\mathbf{y} = \mathbf{r}-\mathbf{r}'$ and $\mathrm{d}^3\mathbf{r} = \mathrm{d}^3\mathbf{y}$. Then, by Fubini's theorem:

$$\begin{aligned}
\tilde{\mathbf{B}}(\mathbf{k}) &= \int_{\mathbb{R}^3} \mathrm{d}^3\mathbf{r}\mathrm{e}^{-\mathrm{i}\mathbf{k}\cdot\mathbf{r}}\mathbf{B}(\mathbf{r}) \\
&= \int_{\mathbb{R}^3}\int_{\mathbb{R}^3} \mathrm{d}^3\mathbf{y}\,\mathrm{d}^3\mathbf{r}'\mathrm{e}^{-\mathrm{i}\mathbf{k}\cdot\mathbf{y}}\mathrm{e}^{-\mathrm{i}\mathbf{k}\cdot\mathbf{r}'}\frac{1-3(\hat{\mathbf{y}}\cdot\hat{\mathbf{z}})^2}{2y^3} \\
&\quad\times[3M_z(\mathbf{r}')\hat{\mathbf{z}} - \mathbf{M}(\mathbf{r}')] \\
&= \int_{\mathbb{R}^3} \mathrm{d}^3\mathbf{y}\frac{1-3(\hat{\mathbf{y}}\cdot\hat{\mathbf{z}})^2}{2y^3}\mathrm{e}^{-\mathrm{i}\mathbf{k}\cdot\mathbf{y}} \\
&\quad\times\left[\int_{\mathbb{R}^3}\mathrm{d}^3\mathbf{r}'[3M_z(\mathbf{r}')\hat{\mathbf{z}} - M(\mathbf{r}')]\mathrm{e}^{-\mathrm{i}\mathbf{k}\cdot\mathbf{r}'}\right] \\
&= \sqrt{\frac{4\pi}{5}}[3\tilde{M}_z(\mathbf{k})\hat{\mathbf{z}} - \tilde{\mathbf{M}}(\mathbf{k})]\int_{\mathbb{R}^3}\mathrm{d}^3\mathbf{y}\mathrm{e}^{-\mathrm{i}\mathbf{k}\cdot\mathbf{y}}Y_2^0(\theta_y)y^{-3},
\end{aligned}$$

where $Y_2^0(\theta_y) = \sqrt{5/16\pi}(3\cos^2\theta_y - 1)$ and $\cos\theta_y = \hat{\mathbf{y}}\cdot\hat{\mathbf{z}}$. Substituting the expansion:

$$\begin{aligned}
\mathrm{e}^{-\mathrm{i}\mathbf{k}\cdot\mathbf{y}} &= 4\pi\sum_{l=0}^{\infty}\sum_{m=-l}^{l}\mathrm{i}^l Y_l^{m*}(\pi-\theta_k,\pi+\phi_k) \\
&\quad\times Y_l^m(\theta_y,\phi_y)j_l(-ky)
\end{aligned} \tag{B.3}$$

and integrating over the angles using $\int_{S^2} Y_l^{m*}Y_{l'}^{m'}\,\mathrm{d}\Omega = \delta_{mm'}\delta_{ll'}$ leaves only one surviving term ($l=2$, $m=0$). Since $\sqrt{(16\pi/5)}Y_2^0(\theta_k) = (3\cos^2\theta_k - 1) = 3(\hat{\mathbf{k}}\cdot\hat{\mathbf{z}})^2 - 1$ and $Y_2^0(\theta_y) = Y_2^{0*}(\theta_y)$, we have that:

$$\begin{aligned}
&-\int_{\mathbb{R}^3}\mathrm{d}^3\mathbf{y}Y_2^{0*}(\pi-\theta_k)Y_2^0(\theta_y)Y_2^{0*}(\theta_y)j_2(ky)y^{-3} \\
&\quad= -\sqrt{\frac{5}{16\pi}}\int_0^\infty \mathrm{d}y y^2 y^{-3}(3\cos^2\theta_k - 1)j_2(-ky) \\
&\quad= \sqrt{\frac{5}{16\pi}}(1-3(\hat{\mathbf{k}}\cdot\hat{\mathbf{z}})^2)\int_0^\infty \mathrm{d}y y^{-1}j_2(-ky).
\end{aligned} \tag{B.4}$$

Using the identity $j_2(\xi) = (\sin\xi)(\xi^{-3} - \xi^{-1}) - (\cos\xi)(3\xi^{-2})$, the last integral evaluates to 1/3. This completes the proof.

References

[1] R. Bowtell, P. Robyr, Structural investigations with the dipolar demagnetizing field in solution NMR, Phys. Rev. Lett. 76 (1996) 4971.

[2] M.H. Levitt, Demagnetization field effects in two-dimensional solution NMR, Concepts Magn. Reson. 8 (1996) 137.

[3] W. Richter, M. Richter, W.S. Warren, H. Merkle, P. Andersen, G. Adriany, K. Ugurbil, Functional magnetic resonance imaging using intermolecular multiple-quantum coherences, Magn. Reson. Imag. 18 (2000) 489–494.

[4] C. Ramanathan, R.W. Bowtell, NMR imaging and structure measurements using the long-range dipolar field in liquids, Phys. Rev. E 66 (2002) 41201–41201.

[5] L.-S. Bouchard, X.-P. Tang, C.-L. Chin, F.W. Wehrli, W.S. Warren, Structural investigations of materials microstructure using intermolecular multiple-quantum coherences, Oral presentation, ENC (Savannah, GA), 44th Annual Meeting, 2003.

[6] S. Kirkpatrick, C.D. Gelatt, M.P. Vecchi, Optimization by simulated annealing, Science 220 (1983) 671–680.

[7] G.S. Fishman, Monte Carlo: Concepts, Algorithms and Applications, Springer, New York, 1996.

[8] T. Enss, S. Ahn, W.S. Warren, Visualization of the dipolar field in solution NMR and MR imaging: three-dimensional structure simulations, Chem. Phys. Lett. 305 (1999) 101–108.

[9] G. Deville, M. Bernier, J.M. Delrieux, NMR multiple echoes observed in solid He-3, Phys. Rev. B 19 (1979) 5666.

[10] T.P. Harrigan, R.W. Mann, Characterization of microstructural anisotropy in orthotropic materials using a second rank tensor, J. Mater. Sci. 19 (1984) 761–767.

[11] S. Torquato, Random Heterogeneous Materials: Microstructure and Macroscopic Properties, Springer, New York, 2002.

[12] R. Bowtell, S. Gutteridge, C. Ramanathan, Imaging the long-range dipolar field in structured liquid state samples, J. Magn. Reson. 150 (2001) 147.

[13] V. Volterra, Theory of Functionals and of Integral and Integro-differential Equations, Dover, New York, 1959.

[14] R.A. Bertlmann, Anomalies in Quantum Field Theory, Oxford, New York, 2000.

[15] C.L.Y. Yeong, S. Torquato, Reconstructing random media, Phys. Rev. E 57 (1998) 495–506.

[16] C.L.Y. Yeong, S. Torquato, Reconstructing random media. ii. Three-dimensional media from two-dimensional cuts, Phys. Rev. E 58 (1998) 224–233.

[17] M.G. Rozman, M. Utz, Efficient reconstructions of multiphase morphologies from correlation functions, Phys. Rev. E 63 (2001) 0667011–06670118.

[18] P.T. Callaghan, Principles of Nuclear Magnetic Resonance Microscopy, Clarendon Press, Oxford, New York, 1991.

[19] R.W. Mair, M.D. Hurlimann, P.N. Sen, L.M. Schwartz, S. Patz, R.L. Walsworth, Tortuosity measurement and the effects of finite pulse widths on xenon gas diffusion NMR studies of porous media, Magn. Reson. Imag. 19 (2001) 345–351.

[20] G. Pavlovskaya, A.K. Blue, S.J. Gibbs, M. Haake, F. Cros, L. Malier, T. Meersmann, Xenon-131 surface sensitive imaging of aerogels in liquid xenon near the critical point, J. Magn. Reson. 137 (1999) 258–264.